

A chromospheric resonance cavity in a sunspot mapped with seismology

David B. Jess^{1,2*}, Ben Snow³, Scott J. Houston¹, Gert J. J. Botha¹, Bernhard Fleck¹, S. Krishna Prasad¹, Andrés Asensio Ramos^{6,7}, Richard J. Morton¹, Peter H. Keys¹, Shahin Jafarzadeh^{1,8,9}, Marco Stangalini^{10,11}, Samuel D. T. Grant¹ and Damian J. Christian^{1,2}

Sunspots are intense collections of magnetic fields that pierce through the Sun's photosphere, with their signatures extending upwards into the outermost extremities of the solar corona¹. Cutting-edge observations and simulations are providing insights into the underlying wave generation², configuration^{3,4} and damping⁵ mechanisms found in sunspot atmospheres. However, the in situ amplification of magneto-hydrodynamic waves⁶, rising from a few hundreds of metres per second in the photosphere to several kilometres per second in the chromosphere⁷, has, until now, proved difficult to explain. Theory predicts that the enhanced umbral wave power found at chromospheric heights may come from the existence of an acoustic resonator^{8–10}, which is created due to the substantial temperature gradients experienced at photospheric and transition region heights¹¹. Here, we provide strong observational evidence of a resonance cavity existing above a highly magnetic sunspot. Through a combination of spectropolarimetric inversions and comparisons with high-resolution numerical simulations, we provide a new seismological approach to mapping the geometry of the inherent temperature stratifications across the diameter of the underlying sunspot, with the upper boundaries of the chromosphere ranging between $1,300 \pm 200$ km and $2,300 \pm 250$ km. Our findings will allow the three-dimensional structure of solar active regions to be conclusively determined from relatively commonplace two-dimensional Fourier power spectra. The techniques presented are also readily suitable for investigating temperature-dependent resonance effects in other areas of astrophysics, including the examination of Earth-ionosphere wave cavities¹².

Spectropolarimetric observations, captured in the Si I 10827 Å and He I 10830 Å lines at high spatial (110 km per pixel), temporal (14.6 s) and spectral (0.04 Å per pixel) resolution, were acquired across the centre of a large sunspot on 14 July 2016 using the Facility Infrared Spectropolarimeter¹³ (FIRS) at the National Science Foundation's Dunn Solar Telescope. Simultaneous contextual imaging is provided by the Rapid Oscillations in the Solar Atmosphere¹⁴ (ROSA) and the Interferometric BIdimensional Spectrometer¹⁵ (IBIS) instruments. Spatially resolved Doppler velocities are derived as a function of time for the entire 86 min data sequence, providing 35,350 individual velocity measurements with amplitudes in the

range of ± 0.3 km s⁻¹ and ± 6 km s⁻¹ for the photospheric Si I 10827 Å and upper-chromospheric He I 10830 Å time series, respectively. The resulting images and spectra (Fig. 1) highlight the persistent and regular wave signatures manifesting in the sunspot umbra.

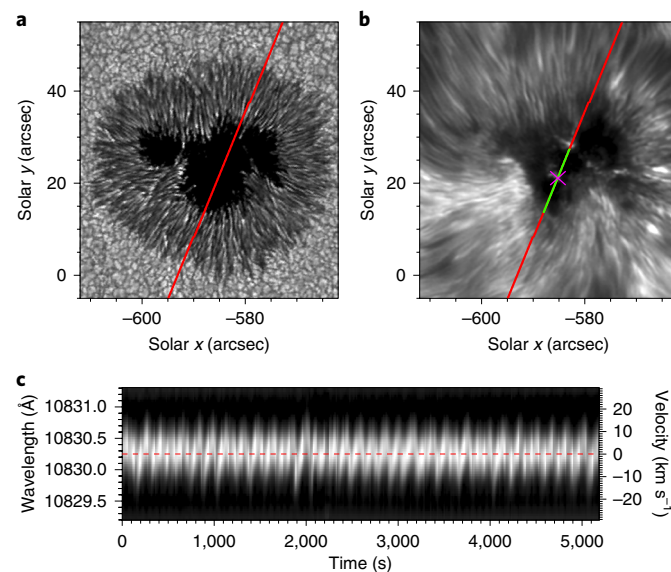


Fig. 1 | The velocity signatures of the magnetized sunspot atmosphere observed on 14 July 2016. **a,b**, ROSA 4170 Å continuum (photosphere; panel **a**) and IBIS 8542 Å line core (chromosphere; panel **b**) images of the sunspot atmosphere at 13:42 UT on 14 July 2016, with the axes displaying the associated heliocentric coordinates. The solid red lines highlight the position of the FIRS slit, while the solid green line indicates the portion of the slit that clearly crosses the chromospheric umbra (that is, not overlapping with penumbra or quiet Sun structures). The pink cross identifies a persistent umbral brightening that segregates the umbral spectra into two distinct regions. **c**, A velocity-time image that documents the spectral and temporal evolution of the He I 10830 Å Stokes I line profile from a single umbral pixel. The black-to-white colour scale represents the inverted spectral intensities to assist with visual clarity, while the horizontal dashed red line indicates the rest position of the He I 10830 Å line core.

¹Astrophysics Research Centre, School of Mathematics and Physics, Queen's University Belfast, Belfast, UK. ²Department of Physics and Astronomy, California State University Northridge, Northridge, CA, USA. ³Centre for Geophysical and Astrophysical Fluid Dynamics, University of Exeter, Exeter, UK.

⁴Department of Mathematics, Physics and Electrical Engineering, Northumbria University, Newcastle upon Tyne, UK. ⁵ESA Directorate of Science, Operations Department, Greenbelt, MD, USA. ⁶Instituto de Astrofísica de Canarias, La Laguna, Tenerife, Spain. ⁷Departamento de Astrofísica, Universidad de La Laguna, La Laguna, Tenerife, Spain. ⁸Institute of Theoretical Astrophysics, University of Oslo, Oslo, Norway. ⁹Rosslund Centre for Solar Physics, University of Oslo, Oslo, Norway. ¹⁰Italian Space Agency (ASI), Rome, Italy. ¹¹INAF-OAR National Institute for Astrophysics, Rome, Italy. *e-mail: d.jess@qub.ac.uk

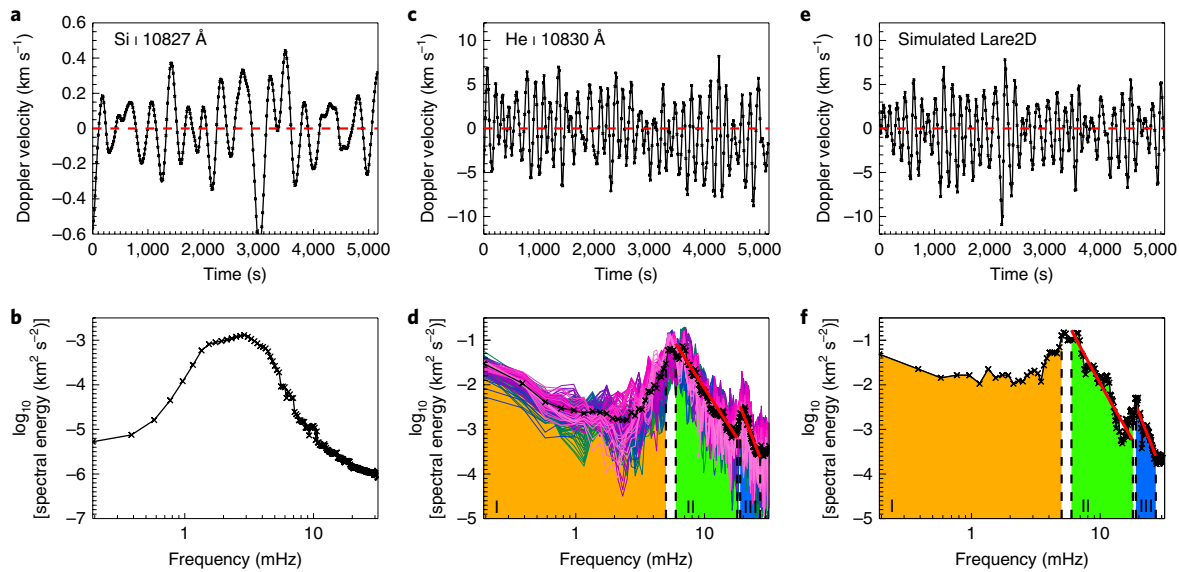


Fig. 2 | Doppler velocities and spectral energies of observed and simulated time series. **a,b**, The Si I 10827 Å (photospheric) Doppler velocity signal for an umbral pixel (**a**), with its corresponding spectral energy displayed on log-log axes (**b**). **c**, The co-spatial He I 10830 Å (upper chromospheric) Doppler velocity signal, where higher-frequency waves are more readily visible when compared with panel **a**. **d**, The calculated He I 10830 Å spectral energies, where the graduated blue-to-pink coloured lines represent spectra derived across the entire sunspot umbral diameter. The solid black line represents the average umbral spectral energy. **e,f**, The simulated velocity time series (**e**), which is extracted from the Lare2D computational domain at an atmospheric height that is compatible with the formation of the He I 10830 Å spectral line, along with its corresponding spectral energy (**f**). The dashed red lines (**a,c,e**) highlight a zero velocity for visual reference. Orange, green and blue shaded regions (bounded by black vertical dashed lines; **d,f**) isolate the spectral energies into regions I (<5 mHz), II (6–17 mHz) and III (18–27 mHz). The solid red lines (**d,f**) highlight the respective maximum-likelihood fits spanning the frequency domains corresponding to regions II and III. The white space between regions I and II acts as a ‘buffer’ since the peak frequency (the beginning of region II) tends to vary throughout the observations. Therefore, we begin fitting the slope at 6 mHz to ensure that any variations are accounted for.

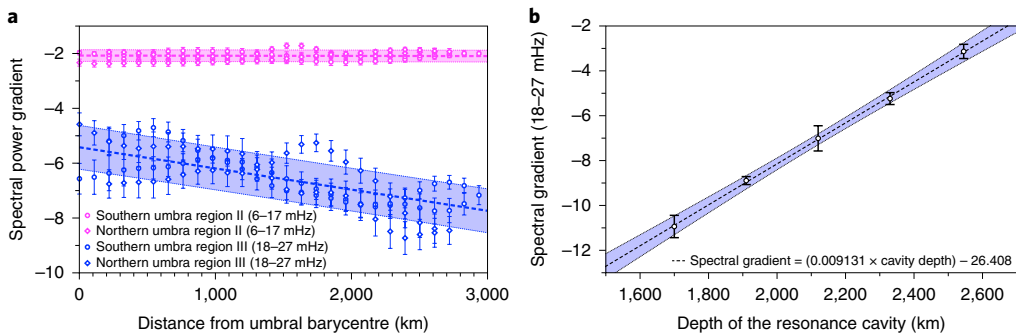


Fig. 3 | Spectral energy gradients of observed and simulated time series. **a**, The spectral power gradients measured for each of the umbral Fourier energy densities, displayed as a function of distance from their associated umbral region barycentre. Here, the magenta and blue colours correspond to regions II (6–17 mHz) and III (18–27 mHz), while the circle and diamond symbols relate to the southward and northward locations in relation to the persistent umbral brightening, respectively. The vertical error bars placed on each data point correspond to the maximum-likelihood 1σ fit uncertainties when measuring the spectral power-law gradients. The dashed magenta and blue lines highlight the linear lines of best fit associated with regions II and III, while the shaded magenta and blue regions identify the standard deviations for the lines of best fit, respectively. **b**, The spectral slopes of region III (18–27 mHz), which are calculated from the maximum-likelihood fits of the Fourier spectral energies produced by Lare2D numerical simulations, as a function of the variable resonance cavity depths imposed in the modelled atmospheres. The vertical error bars highlight the maximum-likelihood 1σ fit uncertainties achieved when measuring the corresponding spectral power-law gradients. The dashed black line maps the linear best-fit line through the data points, while the blue shaded region (bounded by the black dotted lines) highlights the 95% confidence level associated with the fitted line.

A long-lived filamentary structure, consistent with previous observational studies^{16,17}, naturally segregates the sunspot into two distinct umbrae (Fig. 1). The centres of gravity (or barycentres) of each isolated umbra are calculated, allowing the wave characteristics to be studied as a function of distance from their respective umbral core. Fourier spectral energies¹⁸ are computed for each of

the 101 spatial pixels crossing the sunspot umbrae (Fig. 2), revealing distinct differences between the upper-chromospheric He I 10830 Å spectra and their co-spatial photospheric Si I 10827 Å counterparts. Most notable is the fact that all of the He I 10830 Å spectral energies can be categorized by three distinct regions: (region I; <5 mHz) the evanescent regime with frequencies below the acoustic cut-off;

(region II; 6–17 mHz) the region where propagating waves become permissible and demonstrate broad spectral peaks and strong spectral energies that are consistent with previous observational findings¹⁹; and (region III; 18–27 mHz) the final regime where the spectral energy demonstrates a steep power-law relationship with gradient α . It is region III that acts as both an indicator for the presence of a resonant layer⁹, as well as the ability to use the spectral slope, α , as a diagnostic tool for estimating the thickness of the temperature structuring of the chromospheric resonance cavity¹¹.

Fitting the He I 10830 Å spectral energy gradients for region III through maximum-likelihood statistical approaches²⁰ reveals a strong correspondence between the steepness of the slope and the distance subtended from the corresponding umbral barycentre (Fig. 3). While the spectral gradients for region II remain consistent across the entire extent of the sunspot (with characteristic spectral gradients of -2.1 ± 0.2), the spectral slopes for region III vary as a function of distance from their respective umbral barycentre, with gradients as shallow as -5.4 ± 0.6 at the core of the relevant umbra, extending to gradients as steep as -7.8 ± 0.6 at maximal distances ($\sim 3,000$ km) from each barycentre. Spectral slopes of this magnitude closely resemble the strong dissipative ranges previously documented in studies of the solar wind²¹.

To compare with the observational findings, the Lare2D²² numerical nonlinear compressible magnetohydrodynamic (MHD) code, which is employed in a 1.5D configuration, is driven by the photospheric velocity profiles extracted from the observational Si I 10827 Å Doppler shifts and allowed to evolve in time. The embedded atmospheric model is constrained by HAnle and Zeeman Light²³ (HAZEL) inversions applied to the spectropolarimetric data products²⁴, with the computed velocity signals extracted with a cadence of 14.6 s (to match that of the FIRS observations) following propagation of the wave signatures to the upper temperature gradient corresponding to the commencement of the transition region, which is consistent with the predicted formation height of the He I 10830 Å spectral line²⁵. The velocity time series is cropped to 86 min in duration to match that of the observations and converted into spectral energies (Fig. 2e,f). This process is repeated for input atmospheres scaled to 80%, 90%, 110% and 120% of the original temperature stratification height, providing resonance cavity depths (photosphere to the base of the transition region) spanning 1,700–2,545 km. The spectral energies computed for both the modelled and observed time series show similar trends across regions I, II and III (Fig. 2). In particular, the modelled region III demonstrates an identical rise in spectral energy at ~ 20 mHz, before dropping off very rapidly with increasing frequency. Importantly, re-running the numerical simulations for an atmospheric profile devoid of the steep transition region temperature gradient produces spectral energies where the secondary ~ 20 mHz spectral peak is absent. This verifies that the steep temperature gradient intrinsic to the solar transition region, which amplifies the spectral energies at ~ 20 mHz, is required for the initiation of resonance behaviour. The maximum-likelihood fitted spectral slopes for region III reveals that shallower spectral gradients correspond to inherently deeper chromospheric cavities (Fig. 3b), allowing the observed spectral slopes for region III to unveil the cavity depths of the local sunspot atmosphere. Importantly, a larger cavity depth introduces a greater resonant energy content, hence providing more energy across the frequency range, and thus reducing the steepness of the associated spectral slope¹¹.

The range of gradients measured for region III (18–27 mHz) of the sunspot spectral energies span -5.4 ± 0.6 (close to the umbral barycentre) to -7.8 ± 0.6 (at the outermost extremities of the umbra), suggesting that the chromospheric resonance cavity is thickest near the core of the umbra, dropping to its thinnest depth at the penumbral boundary (Fig. 3). The upper geometric height of the chromosphere, τ_{chromo} , which corresponds to the uppermost

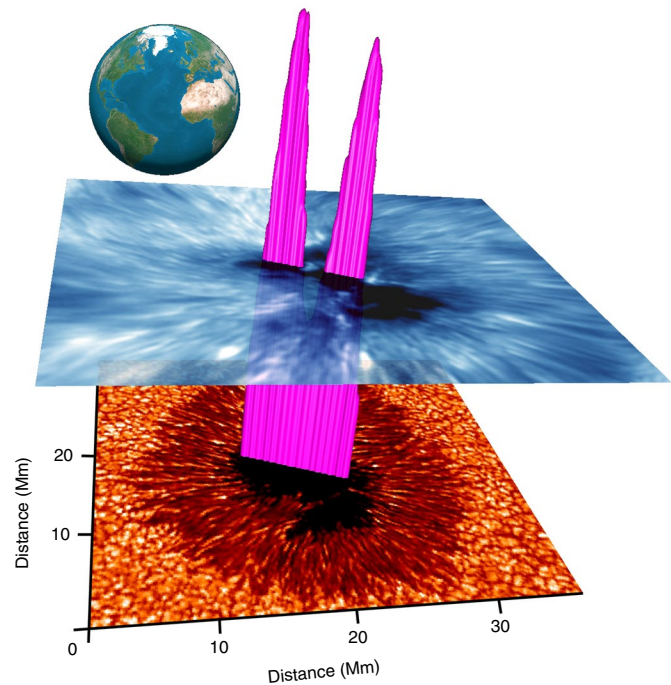


Fig. 4 | Three-dimensional visualization of the geometric extent of the chromosphere above active region NOAA 12565. The geometric extent of the chromosphere, visualized here as the pink isocontours extending upwards from the photospheric (ROSA 4170 Å continuum) umbra and through the chromospheric (IBIS 8542 Å line core). It can be seen that the depth of the resonance cavity is suppressed in the immediate vicinity of the trans-umbral filamentary structure, providing geometric heights of approximately 1,300 km, which is consistent with the depth measured at the outermost edges of the umbra. The cores of the umbrae display the largest resonance cavity depths, often with geometric heights on the order of 2,300 km. An image of the Earth is added to provide a sense of scale. Note that the pink resonance cavity depth contours are not to scale. Credit: Earth image, NOAA.

boundary of the resonance cavity before the commencement of the transition region, can be defined (Fig. 3b) as

$$\tau_{\text{chromo}} = \frac{\text{Region III spectral slope} + 26.408}{0.009131} \cos \theta \quad (1)$$

where θ is the inclination angle of the wave propagation path with respect to the normal to the solar surface. Use of the inclination angle is important since the Lare2D numerical code simulates the wave evolution along a given magnetic field line, which may be inclined with respect to the solar normal. Hence, taking the magnetic field inclinations into consideration allows for the conversion of a wave propagation distance into a true geometric height of the chromosphere for that particular spatial location. Utilizing the vector magnetic fields derived from HAZEL inversions²⁴ yields inclination angles ranging from 0° at the umbral barycentres, through to approximately 50° towards the outer umbral boundaries, providing geometric heights for the upper chromosphere on the order of $2,300 \pm 250$ km and $1,300 \pm 200$ km for the umbral cores and umbral/penumbral boundaries, respectively (Fig. 4).

Here, we show strong evidence substantiating the presence of a chromospheric resonance cavity above a sunspot. We reveal how high-resolution spectropolarimetric observations, when combined with cutting-edge numerical MHD simulations, provide the spectral energy sensitivity necessary to accurately measure the high-frequency spectral gradients that are modulated by the depth of the

chromospheric resonance cavity. Importantly, the variable cavity depths across the diameter of the sunspot have important implications for atmospheric seismology, since the umbral atmosphere can no longer be considered as a homogeneous slab environment. Instead, thicknesses of the chromospheric resonance layer will need to be incorporated into seismological estimations in order to improve the accuracy of such techniques. Looking ahead, fibre-fed spectrographs on the upcoming 4 m Daniel K. Inouye Solar Telescope will provide two-dimensional spectral energy maps of sunspots with unprecedented resolving power, allowing revolutionary three-dimensional atmospheric reconstructions to be uncovered.

Furthermore, the topic of resonance cavities is fundamentally important across a wide range of ongoing astrophysical research including, but not limited to, the examination of near-Earth ionospheric wave cavities¹². As a result, understanding the physics responsible for the creation of resonance cavities, along with their impact on the Universe around us, is of paramount importance. Our results enable the astrophysical community to benchmark, through novel seismological approaches, what atmospheric characteristics are required to form a stable resonance cavity (for example, specific temperature stratifications), what impact this has on waveforms interacting with the cavity structure (for example, power enhancements at well-defined frequencies), and how cutting-edge numerical simulations can be employed alongside high-precision spectropolarimetric data products to deduce physical parameters corresponding to the local plasma conditions (for example, cavity depth).

Methods

Observations. The sunspot at the centre of the active region NOAA 12565 on 14 July 2016 was the primary focus of the observing campaign. The image sequence duration was approximately 86 min, and was obtained during excellent seeing conditions between 13:42–15:08 UT with the Dunn Solar Telescope at Sacramento Peak, New Mexico. The Hydrogen-Alpha Rapid Dynamics camera²⁶ (HARDcam) and ROSA¹⁴ imaging systems were simultaneously used to capture active region NOAA 12565 at G-band, blue continuum (4170 Å), Ca II K and H α wavelengths, which was positioned at heliocentric coordinates (−582°, 30''), providing a heliocentric viewing angle of 38° ($\mu \simeq 0.79$). This location corresponds to N05.2E38.1 in the conventional heliographic coordinate system. To complement the ROSA and HARDcam data streams, the FIRS¹³ slit-based spectrograph and IBIS¹⁵ imaging spectrograph acquired contemporaneous observations of the same active region in the He I 10830 Å and Ca II 8542 Å spectral lines, respectively.

The FIRS instrument was configured to obtain diffraction-limited spectropolarimetry of the He I 10830 Å upper-chromospheric absorption lines by utilizing a 75'' slit length (providing a spatial sampling of 0.15'' per pixel along the slit), combined with a 0.225 slit width. A confined five-step raster was obtained by moving the slit 0.225 after each integration, providing a narrow 75'' \times 1.125 slot-type field of view that passed through the centre of the umbral core. Each spectrum obtained consisted of 12 consecutive additions of the modulation states to increase the signal-to-noise ratio of the relevant Stokes profiles, providing a final cadence equal to 14.6 s. The observations were reduced into science-ready data products using the publicly available National Solar Observatory FIRS pipeline²⁷, ultimately providing a spectral sampling of 0.04 Å for the He I 10830 Å spectra. To assist with the determination of the FIRS slit pointing and alignment, a slit-jaw camera (in sync with the acquisition of each spectrum) was employed alongside the ROSA, HARDcam and IBIS image sequences to allow the precise spatial location and orientation of the FIRS slit to be mapped.

The IBIS system was deployed in imaging mode (that is, no spectropolarimetric information was retrieved) to increase the field of view captured and to decrease the time taken to acquire a spectral scan. A total of 47 discrete, non-equidistant wavelength steps were utilized across the Ca II 8542 Å line profile with a spatial sampling of 0.098 per pixel, providing a circular field of view with a diameter of 97'' and a spectral coverage of 8540.82–8543.42 Å (that is, line core ± 1.3 Å). In total, 543 imaging spectral scans were completed, each with a cadence of 9.4 s. A radial blueshift correction was performed to compensate for the classically mounted etalons²⁸. A white-light camera, in sync with the IBIS narrowband sequences, was employed to de-stretch the resulting spectral scans^{29,30}. Contextual ROSA 4170 Å continuum and IBIS Ca II 8542 Å line core images are displayed in Fig. 1, alongside contours depicting the precise location of the FIRS slit.

Establishing the Doppler velocities. The orientation of the FIRS slit resulted in it crossing an approximate 11 Mm ($\sim 15''$) expanse of the sunspot umbra. This extent is highlighted by a solid green line in Fig. 1b, with pixels beyond this corresponding to penumbral or quiet Sun locations. Each Stokes I spectrum extracted from the sunspot umbra is normalized by its own respective average continuum intensity,

I_c (Extended Data Fig. 1a). When the time-spectral evolution of an umbral pixel is examined (see, for example, Extended Data Fig. 1b), it is clear to see regular periodic wave signals with a characteristic period on the order of 3 min.

It must be noted that the He I spectral window around 10830 Å is actually a collection of three independent electron transitions³¹: $2s^2S_1-2p^3P_0$ at 10829.09 Å, $2s^2S_1-2p^3P_1$ at 10830.25 Å, and $2s^2S_1-2p^3P_2$ at 10830.34 Å. Typically, under conditions where velocity signatures are significantly subsonic^{32,33}, the He I triplet is observed as two absorption features since the 10830.25 Å and 10830.34 Å profiles are fully blended together (forming the deep 'red' component), while the more shallow 'blue' component at 10829.09 Å remains isolated³⁴. It is common practice to perform spectropolarimetric inversions on the blue He I component since it has a higher effective Landé g -factor ($g_{eff} = 2.0$ at 10829.09 Å, versus $g_{eff} = 1.75$ and $g_{eff} = 1.25$ at 10830.25 Å and 10830.34 Å, respectively) and potential blends do not need to be considered. Indeed, the HAZEL inversions performed on this dataset were applied to the blue He I component³⁴. On the other hand, (subsonic) Doppler velocity measurements can be derived more reliably from the red He I component due to its significantly larger line depth and intrinsically better signal-to-noise. For the purpose of establishing Doppler maps of the sunspot umbra, we fit the red component of the He I spectra since the resulting profiles are fully blended, with no evidence of supersonic flows (see, for example, Extended Data Fig. 1a).

By fitting all 35,350 (101 pixels across the 11 Mm umbral diameter and 350 acquisitions in time) He I 10830 Å absorption lines with a Voigt profile³⁵ (a combination of Gaussian and Lorentzian profiles due to the Doppler and pressure broadening sensitivities, respectively, of the He I 10830 Å line), the intrinsic Doppler velocities were mapped. Velocity oscillations with amplitudes in the range of ± 6 km s^{−1} were found to span the entire diameter of the chromospheric sunspot umbra and last throughout the duration of the observing period (see, for example, Extended Data Fig. 1b).

Segregating the umbra into two distinct regions. Within the 11 Mm umbral region, there existed a persistent brightening that was only visible in the chromospheric image sequences obtained by IBIS (Ca II 8542 Å) and HARDcam (H α 6563 Å). The brightening, at approximately 5.6 Mm ($\sim 7.7''$) along the umbral portion of the FIRS slit, is highlighted with a pink cross in Fig. 1b and in Extended Data Fig. 2a. Owing to an absence of this feature in the photospheric observations (see, for example, the ROSA 4170 Å continuum image depicted in Fig. 1a), the chromospheric umbral brightening is likely to be a long-lived filamentary structure^{16,36}. Indeed, from inspection of the time-distance map of the fitted He I Doppler velocities in Extended Data Fig. 1b, the umbral brightening (highlighted using a vertical dashed pink line) exhibits preferential red-shifted Doppler velocities, a characteristic that is consistent with previous observational measurements¹⁷. Extended Data Fig. 2b displays a magnified view of the chromospheric sunspot umbra, where the persistent brightening is better revealed (and highlighted using a pink cross).

To focus our study purely on the umbral signatures, we decomposed the umbral spectra into two distinct regions that are isolated from one another by the long-lived chromospheric filamentary structure crossing the FIRS slit. To do this, we extracted a time-averaged Stokes I / I_c intensity along the umbral portion of the FIRS slit (see, for example, the solid green line in Extended Data Fig. 2b) that corresponds to the He I 10830 Å line core. This intensity profile is plotted in Extended Data Fig. 2c, where the vertical dashed pink line highlights the location of the persistent chromospheric umbral brightening, which demonstrates intensities considerably above the quiescent umbral background. Next, the centres of gravity (or barycentre) for the intensity profile south (that is, < 5.6 Mm) and north (that is, > 5.6 Mm) of the umbral brightening are calculated to be 2.8 Mm and 8.3 Mm, respectively, which are represented by the vertical dashed red lines in Extended Data Fig. 2c. Thus, the green and blue shaded regions in Extended Data Fig. 2c represent the southern and northern umbral regions, respectively, which are isolated from one another by the persistent chromospheric umbral brightening. Now, any signatures extracted from the data can be related directly to a particular umbral region for further characterization, in addition to the distance from their respective umbral barycentre.

Regions present in the Fourier spectra. In accordance with recent theoretical work¹¹, we isolated the spectral energy plots into three distinct regions.

Region I (< 5 mHz)—part of the spectral energy that is governed by the local acoustic cut-off frequency, ω_c , which only allows waves to propagate upwards providing

$$\omega > \omega_c = \frac{c_s}{2H} \sqrt{1 + 2 \frac{\delta H}{\delta z}}$$

where c_s is the local sound speed, z is the atmospheric height and $H = c_s^2/(\gamma g)$ with γ the adiabatic index and g the acceleration due to gravity^{37,38}. Owing to the almost vertical nature of the magnetic field lines at the core of the sunspot umbra²⁴, we chose an upper limit for region I at 5 mHz, which is consistent with other sunspot observations³⁹.

Region II (6–17 mHz)—portion of the spectral energy where propagating waves become permissible (that is, > 5 mHz) and demonstrate broad spectral peaks and strong spectral energies that are consistent with previous observational

findings^{19,40,41}. Here, region II continues from 6–17 mHz (allowing for a buffer region between 5–6 mHz to allow the overall spectrum to reach a peak energy), revealing a gradual decrease in the spectral energy with frequency. The upper boundary of region II is set at 17 mHz, since another peak at frequencies beyond 18 mHz commences the beginning of region III.

Region III (18–27 mHz)—the final regime of the spectral energy corresponds to the range where steep spectral gradient declines are found. This is the region where the spectral energy is proportional to a $f^{-\alpha}$ scaling, where f is the frequency and α is the linear gradient when plotted on log–log axes¹¹. Owing to the 14.6 s cadence of the FIRS observations, the resulting Nyquist frequency is 34 mHz. From examination of the individual spectral energies, white noise fluctuations commence around 28–30 mHz, which was identified by the flattening of the spectral energy beyond these frequencies (Fig. 2d). As a result, we set the upper boundary for region III at 27 mHz to avoid contamination from high-frequency white noise. It is region III that acts as a diagnostic tool for estimating the thickness and temperature structuring of the chromospheric resonance cavity.

It must be noted that the spectral frequency ranges for regions I (<5 mHz), II (6–17 mHz) and III (18–27 mHz) remain fixed throughout the data analyses.

Features visible in the spectral energy maps. Figure 2d displays the spectral energies for all 101 pixels across the sunspot using a graduated blue-to-pink colour scale. While there is scatter in the spectral energy at each component frequency, the general trend remains the same across all umbral pixels, reiterating the usefulness of sub-dividing the spectral energy densities into their constituent regions (that is, regions I, II and III). The mean spectral energy is overplotted in Fig. 2d using a solid black line, along with the maximum-likelihood fitted lines of best fit for regions II and III using solid red lines. It is clear to see that, on average, the maximum-likelihood fitted spectral gradient for region III is steeper than that for region II, as predicted in recent theoretical models¹¹.

It is possible to re-display Fig. 2d, only now preserving the information along the spatial diameter of the chromospheric sunspot umbra. Extended Data Fig. 3 displays a two-dimensional map of the spectral energy, plotted as a function of frequency (x axis) and distance across the umbra (y axis). As with the spectral energies plotted in Fig. 2d, it is clear to see a dominant broad band of peak power at ≈ 5 mHz across the entirety of the umbra. From visual inspection, it is also possible to identify wedge-shaped traces of peak power extending outwards from the north and south umbral barycentres (identified by the horizontal dashed green lines). A black dotted line in Extended Data Fig. 3 tracks the frequency corresponding to the weighted spectral energy centroid (between frequencies of 3–17 mHz) across the entirety of the sunspot umbra. It can be seen that the north/south umbral barycentres correspond to the highest centroid frequency (~ 6.5 mHz or ~ 155 s), while the furthest extremities of each umbral section demonstrate the lowest centroid frequencies (~ 5.0 mHz or ~ 180 s). This type of behaviour is consistent with the umbral barycentres displaying the most vertical magnetic fields, hence pushing the acoustic cut-off frequency to higher values³⁷. A similar phenomenon has also been observed in IBIS spectral imaging observations of umbral oscillations³⁹, and reiterates the appropriateness of defining the start of region II at 6 mHz.

From Extended Data Fig. 3, it is also possible to identify the second enhancement of spectral energy corresponding to region III (≈ 18 mHz or 55 s). Here, there appears to be more pronounced enhancements of spectral energy close to the north/south umbral barycentres (that is, coincident with the horizontal dashed green lines in Extended Data Fig. 3), when compared with similar frequencies at the very extreme edges of the sunspot umbra (for example, distances of approximately 0 Mm and 11 Mm in Extended Data Fig. 3). The spectral energy associated with region III is much weaker than that found in region II, often by 1–2 orders of magnitude (also visible in Fig. 2d). As the spectral gradient present in region III contains information related to the structuring of the underlying umbral resonance cavity, it is important to calculate the spectral slope with a high degree of precision.

Fitting the spectral energy gradients. To calculate the spectral slopes corresponding to regions II and III, maximum-likelihood fitted gradients were computed for each of the 101 spectral energies across the chromospheric umbra. Often, linear lines of best fit are established to determine the spectral slopes of Fourier power spectra⁴². However, the weighted least-squares minimization process assumes that the data to be fitted are normally (Gaussian) distributed⁴⁰, which may not necessarily be the case, especially when the periodogram of a stationary, linear stochastic process naturally follows a χ^2 distribution^{43,44}. As a result, we applied the maximum-likelihood approach²⁰, which has recently been successfully applied to solar wave studies⁴⁵, to calculate the spectral gradients for regions II and III of the 101 spectral energies across the diameter of the sunspot umbra. The spectral gradients for regions II and III, as a function of distance from their respective umbral barycentre, are plotted in Fig. 3a. It is clear that the spectral slopes for region II are relatively constant, with a slope of -2.1 ± 0.2 . Contrarily, the spectral gradients for region III are seen to vary as a function of distance from their respective umbral barycentre, with gradients as shallow as -5.4 ± 0.6 at the core of the relevant umbra, extending to gradients as steep as -7.8 ± 0.6 at maximal distances ($\sim 3,000$ km) from each barycentre.

We believe the gradients displayed for region II in Fig. 3a point towards a universal sunspot characteristic for waves detected in chromospheric spectral

lines. A recent observational examination of the spectral power slopes for an entirely different sunspot, using ground-based images obtained in the Ca II K and H α line cores, found similar spectral gradients (within the 6–17 mHz spectral range) to those presented here⁴². These gradients are steeper than both the f^{-1} and $f^{-5/3}$ relationships that would be expected for granulation (that is, pink) noise patterns⁴⁶ and the Kolomogorov inertial range⁴⁷, respectively. Instead, they more closely resemble the f^{-2} red noise that is linked to the strong viscous dissipative regimes associated with Brownian motion⁴⁸. Region III, on the other hand, has even steeper spectral gradients that more closely resemble the strong dissipative ranges previously documented in studies of the solar wind^{21,49}. Importantly, the steepening of the spectral slopes as one moves away from the umbral barycentres indicates a strong dependency between the value of the spectral gradient and the characteristics of the underlying resonance cavity in which the spectral signatures were generated.

Numerical MHD simulations. The numerical code employed in the current work is based on the well-documented Lare2D²² software. Here, a velocity driver is injected into an atmospheric model, containing realistic temperature and density structuring, allowing the Lare2D code to evolve the idealized nonlinear compressible MHD equations to compute the velocity signatures as a function of distance along the computational domain. The numerical domain covers the vertical range -21 Mm $\leq z \leq 21$ Mm and is resolved by 8,192 grid cells. The upper convection zone is modelled by a polytropic temperature profile and situated at $z < 0$ Mm in the domain. Above $z = 0$ Mm, the temperature profile of sunspot model 'M' is used, which connects smoothly at the transition region with a typical coronal temperature profile⁵¹. Near the upper boundary the temperature profile is flattened (that is, a constant value is used) to create an open boundary at $z = 21$ Mm. An initial equilibrium is obtained by solving the pressure balance equation, and the two horizontal directions of the computational domain are invariant, making the resulting simulation 1.5-dimensional.

In order to make the numerical outputs as realistic as possible, we employed the HAZEL inversions of the umbral barycentre pixels (that is, where the magnetic field inclination angles are approximately 0°) of active region NOAA 12656 (ref. ²⁴) to provide chromospheric plasma constraints, which allow the sunspot model⁵⁰ 'M' to be rescaled across the rest of the computational grid. This resampled sunspot model formed the background atmosphere embedded within the Lare2D code, with the temperature values plotted using a solid black line in Extended Data Fig. 4. It must be noted that the sunspot under current investigation is slightly less magnetic and fractionally hotter than the standard sunspot model⁵⁰ 'M' atmosphere. Comparisons with the outputs of the Very Fast Inversion of the Stokes Vector⁵² (VFISV) algorithm, applied to co-temporal Helioseismic and Magnetic Imager (HMI) vector magnetogram data⁵³ that have a formation height in the low photosphere, reveal maximum umbral magnetic field strengths on the order of 2,000 G, which is consistent with the resampled sunspot models.

Previous theoretical work¹¹ that studied the characteristics of sunspot resonance cavities employed a variety of injected photospheric velocity drivers, including those corresponding to white (f^0), pink (f^{-1}) and red (f^{-2}) noise signatures, which are believed to be representative of the spectral signatures present in the Sun's upper convection zone⁵⁴. However, the spectroscopic observations of active region NOAA 12565 obtained by FIRS allows us to provide a better estimate of the real underlying photospheric velocity signal. Extracting bisector velocities of the Si I 10827 Å absorption feature at 20% of the maximum line depth provides photospheric velocities that correspond to an optical depth of $\log(\tau_{500\text{nm}}) \sim -0.65$, or ~ 50 km above the photospheric layer (ref. ⁵⁰ and S. J. González Manrique et al., manuscript in preparation). The extracted Si I 10827 Å velocity signatures have peak amplitudes on the order of 300 m s⁻¹ (Fig. 2a), which is consistent with previous sunspot oscillation studies⁵⁵. These photospheric velocity perturbations are rescaled and applied at the lower ($z = -21$ Mm) boundary of the Lare2D code and allowed to evolve. The rescaling is to ensure that the wave root mean square (r.m.s.) amplitudes produced by the simulations at $z = 0$ Mm (that is, the photosphere) are consistent with the observed Si I 10827 Å profile fluctuations.

Data interpretation. The velocity outputs from the Lare2D simulation were extracted at a cadence of 14.6 s (to match that of the FIRS observations) at an atmospheric height of 2,120 km (vertical dotted black line in Extended Data Fig. 4), which is consistent with the approximate formation height of the He I 10830 Å spectral line^{25,56}. The velocity time series was then cropped to 86 min in duration (again, to match that of the observations) and converted into spectral energies by following the same methodology applied to the FIRS He I 10830 Å data. There are a number of distinct similarities between the observed and simulated velocity time series (Fig. 2c,e). First, both the observed and simulated time series appear modulated by a long-term trend. Such long-period modulation has been extensively observed in magnetoacoustic wave studies^{57–59}, which is normally explained as a consequence of beat phenomena created by the superposition of a number of closely spaced frequencies⁶⁰. This observed phenomenon further supports the presence of a chromospheric resonance cavity, since it has been theoretically shown⁶¹ that long-term modulating periods can be created in the confines of resonant filters. Second, the velocity amplitudes corresponding to the modelled (r.m.s. = 3.2 km s⁻¹) and observed (r.m.s. = 3.5 km s⁻¹) upper

chromosphere are very similar, demonstrating that the wave amplification process is accurately accounted for in the Lare2D model. Finally, the spectral energies computed for both the modelled and observed time series show similar trends across regions I, II and III. In particular, the modelled region I also displays the relatively flat spectral energy that is consistent with the presence of evanescent waves. Next, the modelled region II reveals a similar peak wave energy at ~ 5 mHz, followed by a gradual decline in spectral energy with a maximum-likelihood fitted gradient equal to -2.3 ± 0.3 . As per the observed spectral gradients for region II (see the magenta data points in Fig. 3a), the modelled values also closely map to the presence of red noise (that is, f^{-2}). Lastly, the modelled region III demonstrates an identical rise in spectral energy at ~ 20 mHz (~ 50 s), before dropping off very rapidly with increasing frequency.

Importantly, however, the blue data points in Fig. 3a indicate that the spectral slope associated with region III varies as a function of distance away from the umbral barycentre. Theoretical work¹¹ has revealed that the thickness of the chromospheric resonance cavity has implications for the steepness of the measured spectral gradient, with shallower resonance cavities demonstrating steeper spectral slopes than their thicker cavity counterparts. To investigate this effect further, the thickness (that is, atmospheric height span) of the resonance cavity was rescaled at 80%, 90%, 110% and 120% of the original depth (Extended Data Fig. 4), providing the atmospheric parameters detailed in Extended Data Fig. 5. For each resonance cavity thickness, the numerical models were recomputed, with the spectral energies calculated and the corresponding spectral gradients measured using an identical maximum-likelihood approach. Utilizing the stratified temperature profiles listed in Extended Data Fig. 5, the computed spectral slopes for region III can be plotted as a function of the magnetoacoustic wave propagation distances (Extended Data Fig. 6). It can be seen that larger wave propagation distances (that is, increased cavity depths) introduce a greater resonant energy content, hence providing more energy across the frequency range, and thus reducing the steepness of the associated spectral slope.

The general trends depicted in Fig. 3 and Extended Data Fig. 6 are consistent with previous modelling efforts¹, whereby deeper resonance cavities produce inherently shallower spectral gradients in region III (18–27 mHz). Of course, it must be noted that Fig. 3 and Extended Data Fig. 6 depict the variations in the spectral slopes as a function of the distance over which the magnetoacoustic waves propagate. In an idealized case, where the magnetic fields are aligned with the normal to the solar surface, these propagation distances will be identical to the geometric height of the upper chromosphere. On the other hand, if the magnetic field lines are inclined to the solar normal, then this angle will need to be incorporated into the calculation to estimate the true geometric height of the upper chromosphere in that location. With this in mind, it becomes possible to estimate the depth of the chromospheric resonance cavity for each location within the sunspot umbra simply by comparing the measured spectral slope of region III to the reference spectral energies computed via the Lare2D numerical models.

Here, we have utilized the presence of a spectral energy peak at ~ 20 mHz (that is, region III; see Fig. 2d) as an indicator of a resonance cavity existing in our observational and simulated data, which is consistent with theoretical and numerical investigations documented in recent years^{9,11}. However, to confirm that a resonance cavity is the mechanism responsible for the elevated spectral energies in the range of 18–27 mHz, we created an independent numerical test whereby the Lare2D simulations were re-run for a background atmosphere devoid of the steep transition region temperature gradient. For this test, the temperature reached the chromospheric plateau value ($\sim 6,000$ K; see Extended Data Fig. 4) at an atmospheric height of 0 km, then remained constant through to the upper boundary of the simulation domain, hence removing the conditions necessary for an acoustic resonator to operate (that is, the temperature gradient synonymous with the transition region).

The resulting spectral energies (Extended Data Fig. 7) reveal how removing the transition region entirely from the model atmosphere produces a shallower spectral gradient following the ~ 5 mHz peak. This is likely a consequence of the flattened temperature profile modifying the acoustic cut-off frequency with atmospheric height, hence resulting in a different distribution of energies across the frequency spectrum⁶. Importantly, removing the steep temperature gradient inherent to the solar transition region, which is believed to be required for the initiation of resonance behaviour¹¹, acts to alleviate the rise in spectral energies at ~ 20 mHz. As a result, we conclude that the heightened spectral energies contained within the observed and simulated region III (18–27 mHz; Fig. 2) are a direct consequence of the lower (photospheric) and upper (transition region) temperature gradients intrinsic to the solar atmosphere, hence giving rise to the creation of a resonance cavity.

The range of gradients measured for region III (18–27 mHz) of the sunspot spectral energies span -5.4 ± 0.6 (close to the umbral barycentre) to -7.8 ± 0.6 (at the outermost extremities of the umbra). Immediately, this suggests that the chromospheric resonance cavity is thickest near the core of the umbra, dropping to its thinnest depth at the penumbral boundary. Extended Data Fig. 6 allows the wave propagation distance, τ_{prop} , to be defined as

$$\tau_{\text{prop}} = \frac{\text{Region III spectral slope} + 26.408}{0.009131}$$

where 0.009131 is the gradient of the dashed black line and 26.408 is the intercept on the y axis (Extended Data Fig. 6). The extreme values of the measured spectral

slopes, -7.8 and -5.4 , provide wave propagation distances on the order of 2,035 km and 2,300 km, respectively (shaded magenta and green regions in Extended Data Fig. 6).

However, the magnetic fields spanning the diameter of the sunspot umbral chromosphere are not all vertical in nature (Extended Data Fig. 8). Examining the magnetic field inclination angles, θ , derived from HAZEL inversions applied to the He I 10830 Å spectropolarimetric data reveals that the umbral cores have the most vertical magnetic fields (approximately 0°), while the outermost extremities of the umbrae demonstrate the most inclined magnetic fields (approximately 35 – 50° on average). Furthermore, the filamentary structure that segregates the sunspot into two isolated umbrae displays increased inclination angles approaching 40° (located at approximately 5.6 Mm along the FIRS slit in Extended Data Fig. 8).

As a result, the stratified wave propagation path lengths (Extended Data Fig. 4) are tilted from the solar normal by the inclination angle, θ , which needs to be taken into consideration when estimating the true atmospheric height of the upper chromospheric boundary. As such, the true geometric height of the upper chromosphere, τ_{chromo} , can be defined as

$$\tau_{\text{chromo}} = \frac{\text{Region III spectral slope} + 26.408 \cos \theta}{0.009131} = \tau_{\text{prop}} \cos \theta$$

Utilizing the spatially resolved inclination angles and spectral gradients provides true geometric heights of the upper boundary of the umbral cavity spanning $1,300 \pm 200$ km (spectral slope of -7.8 ± 0.6 and an inclination angle of approximately 50° ; outer umbral edge) through to $2,300 \pm 250$ km (spectral gradient of -5.4 ± 0.6 and a vertically orientated magnetic field; umbral barycentre). This can be visualized graphically in Fig. 4, where the pink isocontours represent the geometric height of the upper chromospheric boundary across the diameter of the sunspot umbra.

Data availability

The data used in this paper are from the observing campaign entitled ‘The Influence of Magnetism on Solar and Stellar Atmospheric Dynamics’ (NSO-SP proposal T1081; principal investigator: D.B.J.), which employed the ground-based Dunn Solar Telescope, USA, during July 2016. Additional supporting observations were obtained from the publicly available NASA’s Solar Dynamics Observatory (<https://sdo.gsfc.nasa.gov>) data archive, which can be accessed via <http://jsoc.stanford.edu/ajax/lookdata.html>. The data that support the plots within this paper and other findings of this study are available from the corresponding author upon reasonable request.

Code availability

The numerical code (Lare2D) used in the work can be downloaded from: <https://warwick.ac.uk/fac/sci/physics/research/cfsa/people/tda/larexd/>.

Received: 26 April 2019; Accepted: 16 October 2019;

Published online: 2 December 2019

References

- Borrero, J. M. & Ichimoto, K. Magnetic structure of sunspots. *Living Rev. Solar Phys.* **8**, 4 (2011).
- Bogdan, T. J. et al. Waves in the magnetized solar atmosphere. II. Waves from localized sources in magnetic flux concentrations. *Astrophys. J.* **599**, 626–660 (2003).
- Lites, B. W., Thomas, J. H., Bogdan, T. J. & Cally, P. S. Velocity and magnetic field fluctuations in the photosphere of a sunspot. *Astrophys. J.* **497**, 464–482 (1998).
- Nagashima, K. et al. Observations of sunspot oscillations in G band and CaII H line with Solar Optical Telescope on Hinode. *Publ. Astron. Soc. Jpn* **59**, S631–S636 (2007).
- Grant, S. D. T. et al. Alfvén wave dissipation in the solar chromosphere. *Nat. Phys.* **14**, 480–483 (2018).
- Kobanov, N. I. & Makarchik, D. V. Propagating waves in the sunspot umbra chromosphere. *Astron. Astrophys.* **424**, 671–675 (2004).
- Tziotziou, K., Tsipropoulou, G., Mein, N. & Mein, P. Dual-line spectral and phase analysis of sunspot oscillations. *Astron. Astrophys.* **463**, 1153–1163 (2007).
- Hollweg, J. V. A new resonance in the solar atmosphere. I. Theory. *Sol. Phys.* **62**, 227–240 (1979).
- Botha, G. J. J., Arber, T. D., Nakariakov, V. M. & Zhugzhda, Y. D. Chromospheric resonances above sunspot umbrae. *Astrophys. J.* **728**, 84 (2011).
- Felipe, T. Origin of the chromospheric three-minute oscillations in sunspot umbrae. *Astron. Astrophys.* **627**, A169 (2019).
- Snow, B., Botha, G. J. J. & Régnier, S. Chromospheric seismology above sunspot umbrae. *Astron. Astrophys.* **580**, A107 (2015).
- Toledo-Redondo, S., Salinas, A., Fornieles, J., Portí, J. & Lichtenegger, H. I. M. Full 3-D TLM simulations of the Earth-ionosphere cavity: effect of conductivity on the Schumann resonances. *J. Geophys. Res. Space Phys.* **121**, 5579–5593 (2016).

13. Jaeggli, S. A. et al. FIRS: a new instrument for photospheric and chromospheric studies at the DST. *Mem. Soc. Astron. Ital.* **81**, 763 (2010).
14. Jess, D. B. et al. ROSA: a high-cadence, synchronized multi-camera solar imaging system. *Sol. Phys.* **261**, 363–373 (2010).
15. Cavallini, F. IBIS: a new post-focus instrument for solar imaging spectroscopy. *Sol. Phys.* **236**, 415–439 (2006).
16. Socas-Navarro, H., McIntosh, S. W., Centeno, R., de Wijn, A. G. & Lites, B. W. Direct imaging of fine structure in the chromosphere of a sunspot umbra. *Astrophys. J.* **696**, 1683–1688 (2009).
17. Beck, C., Choudhary, D. P. & Rezaei, R. A three-dimensional view of the thermal structure in a super-penumbral canopy. *Astrophys. J.* **788**, 183 (2014).
18. Stull, R. *An Introduction to Boundary Layer Meteorology* (Atmospheric and Oceanographic Sciences Library, Springer, 2012).
19. Reznikova, V. E., Shibasaki, K., Sych, R. A. & Nakariakov, V. M. Three-minute oscillations above sunspot umbra observed with the Solar Dynamics Observatory/Atmospheric Imaging Assembly and Nobeyama Radioheliograph. *Astrophys. J.* **746**, 119 (2012).
20. Barret, D. & Vaughan, S. Maximum likelihood fitting of X-ray power density spectra: application to high-frequency quasi-periodic oscillations from the neutron star X-ray binary 4U1608-522. *Astrophys. J.* **746**, 131 (2012).
21. He, J., Wang, L., Tu, C., Marsch, E. & Zong, Q. Evidence of Landau and cyclotron resonance between protons and kinetic waves in solar wind turbulence. *Astrophys. J. Lett.* **800**, L31 (2015).
22. Arber, T. D., Longbottom, A. W., Gerrard, C. L. & Milne, A. M. A staggered grid, Lagrangian-Eulerian remap code for 3-D MHD simulations. *J. Comput. Phys.* **171**, 151–181 (2001).
23. Asensio Ramos, A., Trujillo Bueno, J. & Landi Degl'Innocenti, E. Advanced forward modeling and inversion of Stokes profiles resulting from the joint action of the Hanle and Zeeman effects. *Astrophys. J.* **683**, 542–565 (2008).
24. Houston, S. J. et al. The magnetic response of the solar atmosphere to umbral flashes. *Astrophys. J.* **860**, 28 (2018).
25. Avrett, E. H., Fontenla, J. M. & Loeser, R. Formation of the solar 10830 Å line. In *Infrared Solar Physics* Vol. 154 (eds Rabin, D. M. et al.) 35–47 (IAU Symposium, 1994).
26. Jess, D. B. et al. The source of 3 minute magnetoacoustic oscillations in coronal fans. *Astrophys. J.* **757**, 160 (2012).
27. Derk, A., Beck, C. & Martínez Pillet, V. Inferring telescope polarization properties through spectral lines without linear polarization. *Astron. Astrophys.* **615**, A22 (2018).
28. Cauzzi, G. et al. The solar chromosphere at high resolution with IBIS. I. New insights from the Ca II 854.2 nm line. *Astron. Astrophys.* **480**, 515–526 (2008).
29. Jess, D. B., Mathioudakis, M., Christian, D. J., Crockett, P. J. & Keenan, F. P. A study of magnetic bright points in the Na I D₁ line. *Astrophys. J. Lett.* **719**, L134–L139 (2010).
30. Stangalini, M., DelMoro, D., Berrilli, F. & Jefferies, S. M. MHD wave transmission in the Sun's atmosphere. *Astron. Astrophys.* **534**, A65 (2011).
31. Lagg, A., Woch, J., Solanki, S. K. & Krupp, N. Supersonic downflows in the vicinity of a growing pore. Evidence of unresolved magnetic fine structure at chromospheric heights. *Astron. Astrophys.* **462**, 1147–1155 (2007).
32. Aznar Cuadrado, R., Solanki, S. K. & Lagg, A. Velocity distribution of chromospheric downflows. In *Modern Solar Facilities, Advances in Solar Science* (eds Kneer, F. et al.) 173–176 (2007).
33. González Manrique, S. J. et al. Fitting peculiar spectral profiles in He I 10830 Å absorption features. *Astron. Nachr.* **337**, 1057–1063 (2016).
34. González Manrique, S. J. et al. Temporal evolution of arch filaments as seen in He I 10 830 Å. *Astron. Astrophys.* **617**, A55 (2018).
35. Zaghoul, M. R. On the calculation of the Voigt line profile: a single proper integral with a damped sine integrand. *Mon. Not. R. Astron. Soc.* **375**, 1043–1048 (2007).
36. Henriques, V. M. J. et al. Stable umbral chromospheric structures. *Astron. Astrophys.* **574**, A131 (2015).
37. Bel, N. & Leroy, B. Analytical study of magnetoacoustic gravity waves. *Astron. Astrophys.* **55**, 239 (1977).
38. Roberts, B. MHD waves in the solar atmosphere. In *Waves, Oscillations and Small-Scale Transients Events in the Solar Atmosphere: Joint View from SOHO and TRACE (SOHO 13)* Vol. 547 (ed. Lacoste, H.) 1 (ESA Special Publication, 2004).
39. Löhner-Böttcher, J., BelloGonzález, N. & Schmidt, W. Magnetic field reconstruction based on sunspot oscillations. *Astron. Nachr.* **337**, 1040–1044 (2016).
40. Jess, D. B. et al. Solar coronal magnetic fields derived using seismology techniques applied to omnipresent sunspot waves. *Nat. Phys.* **12**, 179–185 (2016).
41. Jess, D. B. et al. An inside look at sunspot oscillations with higher azimuthal wavenumbers. *Astrophys. J.* **842**, 59 (2017).
42. Krishna Prasad, S. et al. The frequency-dependent damping of slow magnetoacoustic waves in a sunspot umbral atmosphere. *Astrophys. J.* **847**, 5 (2017).
43. Groth, E. J. Probability distributions related to power spectra. *Astrophys. J. Suppl. Ser.* **29**, 285–302 (1975).
44. Papadakis, I. E. & Lawrence, A. Improved methods for power spectrum modelling of red noise. *Mon. Not. R. Astron. Soc.* **261**, 612–624 (1993).
45. Morton, R. J., Weberg, M. J. & McLaughlin, J. A. A basal contribution from p-modes to the Alfvénic wave flux in the Sun's corona. *Nat. Astron.* **3**, 223–229 (2019).
46. Matthaeus, W. H. et al. Density and magnetic field signatures of interplanetary 1/f noise. *Astrophys. J. Lett.* **657**, L121–L124 (2007).
47. Huang, S. Y., Hadid, L. Z., Sahaoui, F., Yuan, Z. G. & Deng, X. H. On the existence of the Kolmogorov inertial range in the terrestrial magnetosheath turbulence. *Astrophys. J. Lett.* **836**, L10 (2017).
48. Sheikholeslami, M., Abelman, S. & Ganji, D. D. Numerical simulation of MHD nanofluid flow and heat transfer considering viscous dissipation. *Int. J. Heat Mass Transfer* **79**, 212–222 (2014).
49. Goldstein, M. L., Roberts, D. A. & Fitch, C. A. Properties of the fluctuating magnetic helicity in the inertial and dissipation ranges of solar wind turbulence. *J. Geophys. Res.* **99**, 11519–11538 (1994).
50. Maltby, P. et al. A new sunspot umbral model and its variation with the solar cycle. *Astrophys. J. Suppl. Ser.* **306**, 284–303 (1986).
51. Avrett, E. H. & Loeser, R. Models of the solar chromosphere and transition region from SUMER and HRTS observations: formation of the extreme-ultraviolet spectrum of hydrogen, carbon, and oxygen. *Astrophys. J. Suppl. Ser.* **175**, 229–276 (2008).
52. Borrero, J. M. et al. VFISV: Very Fast Inversion of the Stokes Vector for the Helioseismic and Magnetic Imager. *Sol. Phys.* **273**, 267–293 (2011).
53. Schou, J. et al. Design and ground calibration of the Helioseismic and Magnetic Imager (HMI) instrument on the Solar Dynamics Observatory (SDO). *Sol. Phys.* **275**, 229–259 (2012).
54. Rabello-Soares, M. C., Roca Cortes, T., Jimenez, A., Andersen, B. N. & Appourchaux, T. An estimate of the solar background irradiance power spectrum. *Astron. Astrophys.* **318**, 970–974 (1997).
55. Felipe, T., Khomenko, E., Collados, M. & Beck, C. Multi-layer study of wave propagation in sunspots. *Astrophys. J.* **722**, 131–144 (2010).
56. Vernazza, J. E., Avrett, E. H. & Loeser, R. Structure of the solar chromosphere. III. Models of the EUV brightness components of the quiet-sun. *Astrophys. J. Suppl. Ser.* **45**, 635–725 (1981).
57. Centeno, R., Collados, M. & Trujillo Bueno, J. Spectropolarimetric investigation of the propagation of magnetoacoustic waves and shock formation in sunspot atmospheres. *Astrophys. J.* **640**, 1153–1162 (2006).
58. Centeno, R., Collados, M. & Trujillo Bueno, J. Wave propagation and shock formation in different magnetic structures. *Astrophys. J.* **692**, 1211–1220 (2009).
59. Krishna Prasad, S., Jess, D. B. & Khomenko, E. On the source of propagating slow magnetoacoustic waves in sunspots. *Astrophys. J. Lett.* **812**, L15 (2015).
60. Marsh, M. S. & Walsh, R. W. p-Mode propagation through the transition region into the solar corona. I. Observations. *Astrophys. J.* **643**, 540–548 (2006).
61. Zhukov, V. I. Oscillations on the Sun in regions with a vertical magnetic field. II. On the calculation of the sunspot umbral oscillations. *Astron. Astrophys.* **433**, 1127–1132 (2005).
62. Zhugzhda, Y. D. Three-minute oscillations in sunspots: seismology of sunspot atmospheres. *Astron. Lett.* **33**, 622–643 (2007).

Acknowledgements

D.B.J. would like to thank the UK Science and Technology Facilities Council (STFC) for an Ernest Rutherford Fellowship, in addition to a dedicated standard grant that allowed this project to be undertaken. D.B.J. and S.D.T.G. also wish to thank Invest NI and Randox Laboratories Ltd for the award of a Research & Development Grant (059RDEN-1) that allowed the computational techniques employed to be developed. B.S. is supported by STFC research grant ST/R000891/1. S.K.P. wishes to thank the UK STFC for support. A.A.R. is grateful to the Spanish Ministry of Economy and Competitiveness through project AYA2014-60476-P. S.J. acknowledges support from the European Research Council under the European Union's Horizon 2020 research and innovation programme (grant agreement no. 682462) and from the Research Council of Norway through its Centres of Excellence scheme (project no. 262622). M.S. is grateful for funding received from the European Research Council under the European Union's Horizon 2020 Framework Programme for Research and Innovation, grant agreements H2020 PRE-EST (no. 739500) and H2020 SOLARNET (no. 824135), in addition to support from INAF Istituto Nazionale di Astrofisica (PRIN-INAF-2014). D.J.C. would like to thank California State University Northridge for start-up funding. The Dunn Solar Telescope at Sacramento Peak/NM was operated by the National Solar Observatory (NSO). NSO is operated by the Association of Universities for Research in Astronomy (AURA), Inc., under cooperative agreement with the National Science Foundation (NSF). The SDO/AIA imaging employed in this work are courtesy of NASA/SDO and the AIA, EVE and HMI science teams. We wish to acknowledge scientific discussions with the Waves in the Lower Solar Atmosphere (WaLSA; <https://www.WaLSA.team>)

team, which is supported by the Research Council of Norway (project no. 262622). Imagery was produced by the Visualization and Analysis Platform for atmospheric, Oceanic and solar Research (VAPOR; <https://www.vapor.ucar.edu>), a product of the Computational Information Systems Laboratory at the National Center for Atmospheric Research.

Author contributions

D.B.J. and D.J.C. designed the observational instrumentation set-up. D.B.J., S.J.H. and S.K.P. undertook the ground-based observations. D.B.J., S.J.H., A.A.R. and S.D.T.G. performed analysis of the observations. B.S. and G.J.J.B. designed and carried out numerical MHD simulations. D.B.J., B.S., S.J.H., G.J.J.B., S.K.P., P.H.K., S.J., M.S., B.F. and R.J.M. interpreted the observations and simulations. D.B.J., B.S., S.J.H., R.J.M. and S.D.T.G. prepared and processed all data products. All authors discussed the results and commented on the manuscript.

Competing interests

The authors declare no competing interests.

Additional information

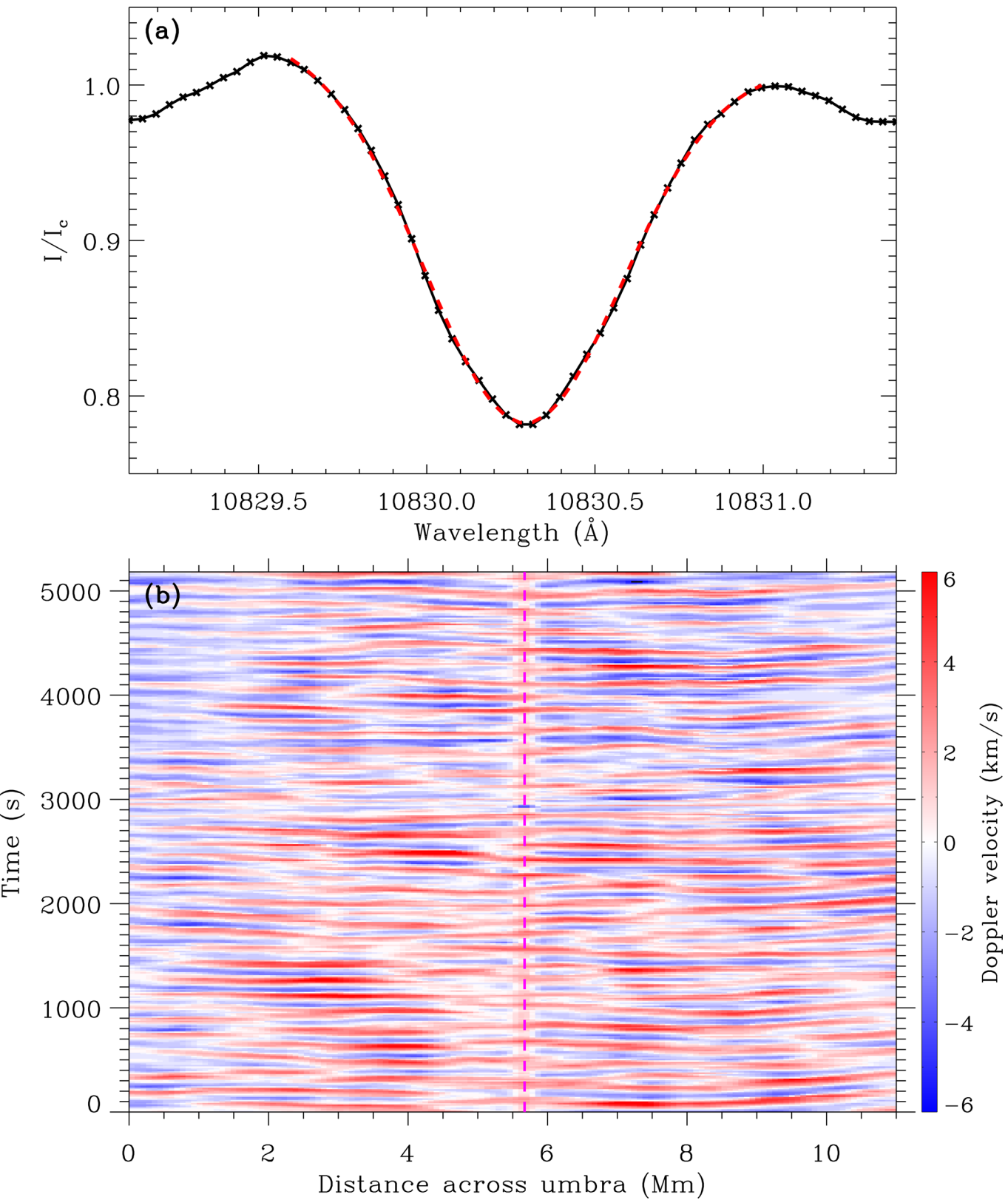
Extended data is available for this paper at <https://doi.org/10.1038/s41550-019-0945-2>.

Supplementary information is available for this paper at <https://doi.org/10.1038/s41550-019-0945-2>.

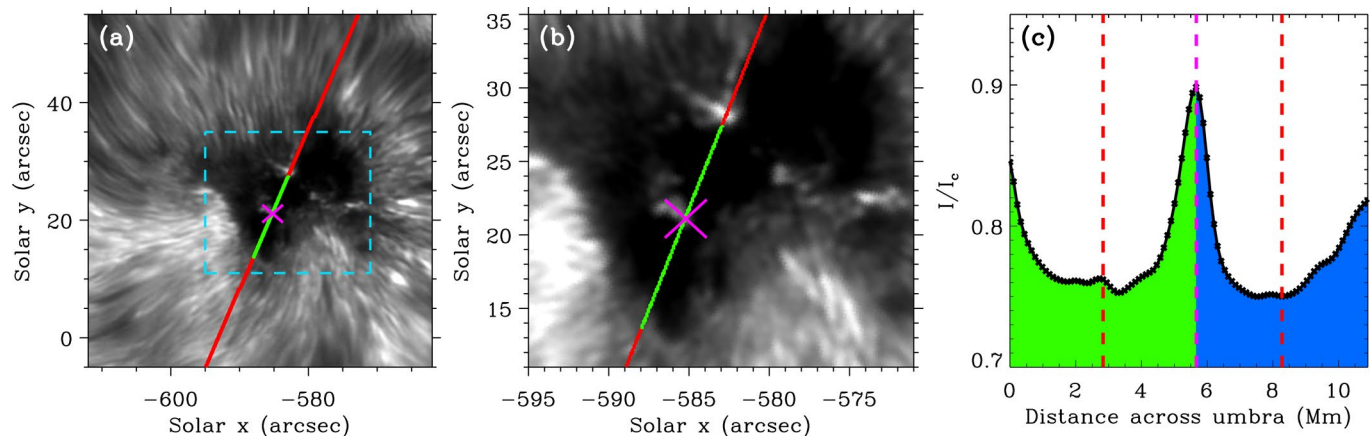
Correspondence and requests for materials should be addressed to D.B.J.

Reprints and permissions information is available at www.nature.com/reprints.

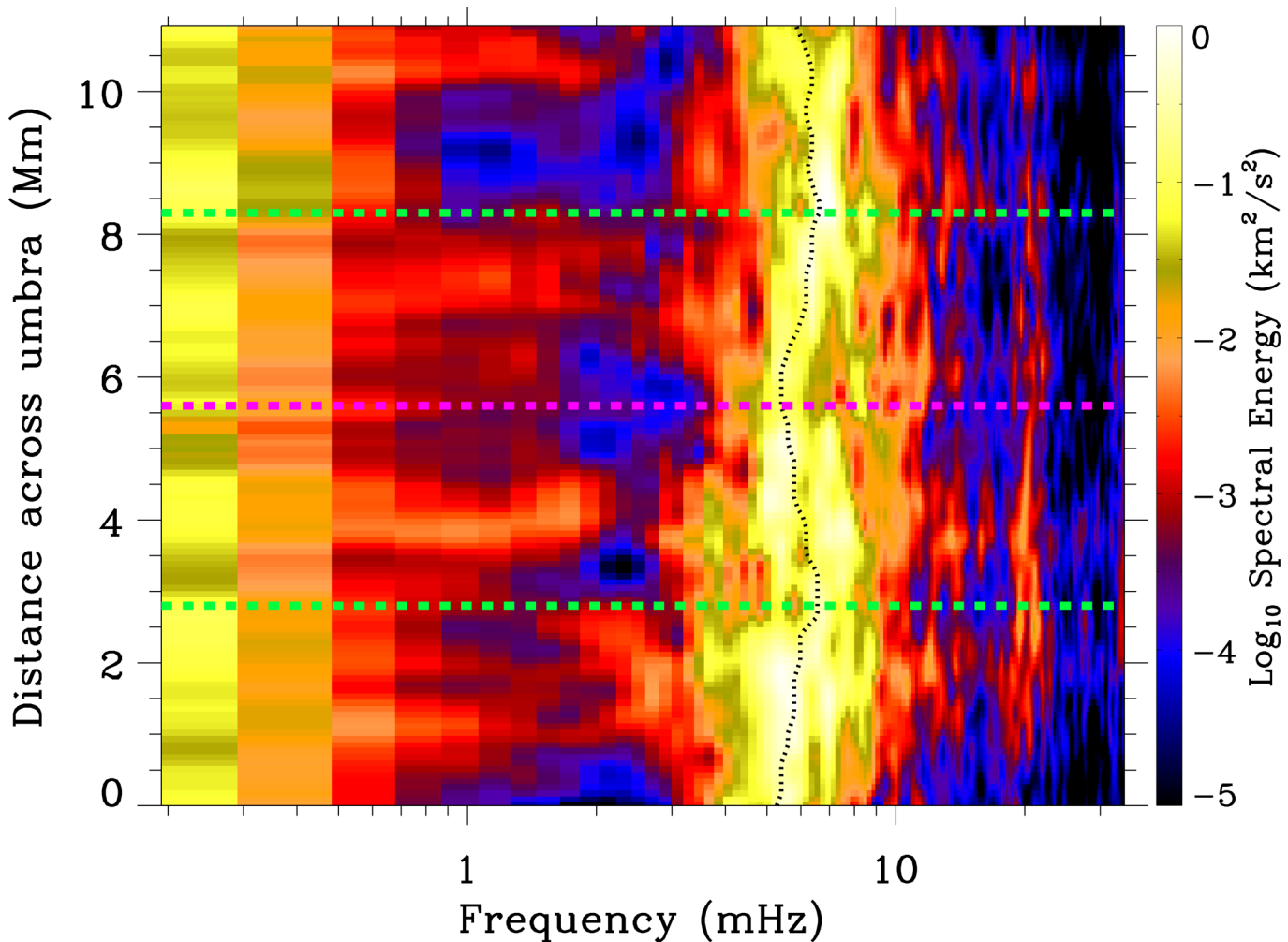
Publisher's note Springer Nature remains neutral with regard to jurisdictional claims in published maps and institutional affiliations. © The Author(s), under exclusive licence to Springer Nature Limited 2019



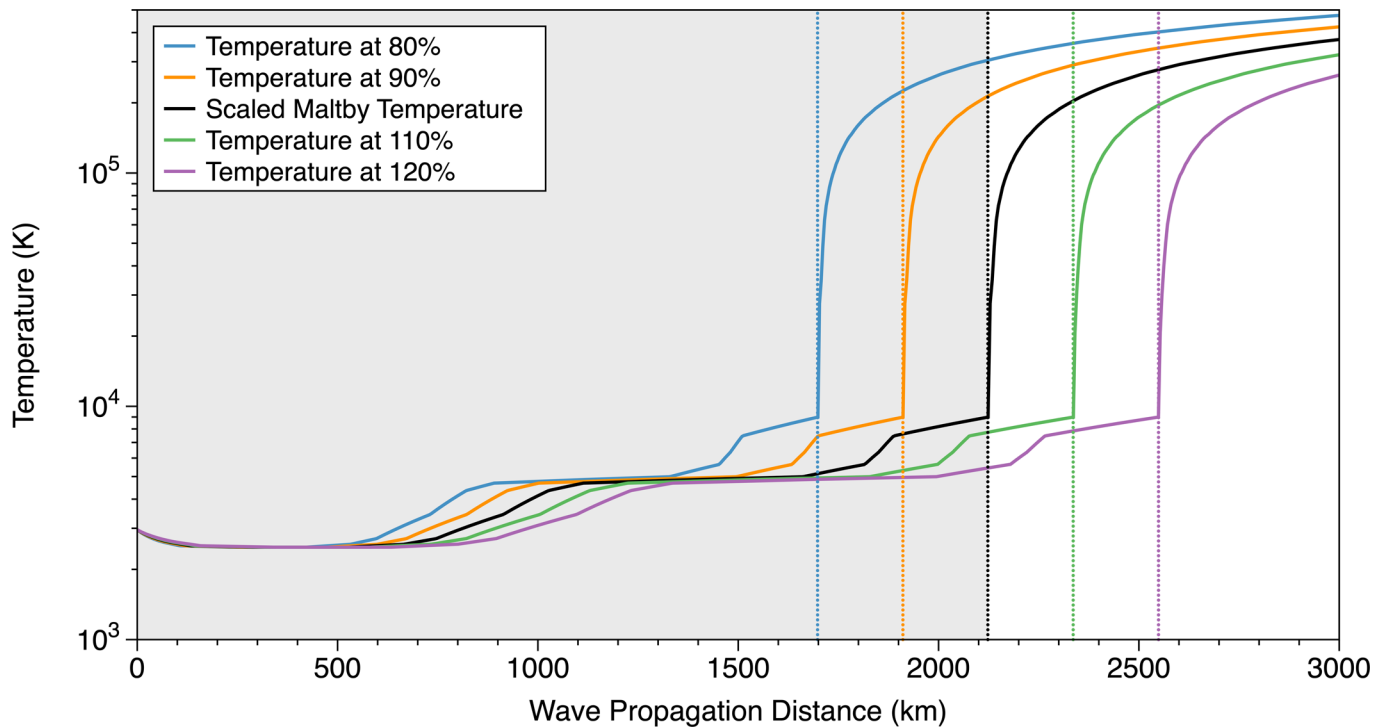
Extended Data Fig. 1 | Omnipresent wave motion observed in He I 10830 Å Doppler velocities. **(a)** A sample umbral He I Stokes / line profile, normalised by the average continuum intensity, I_c , is presented as a solid black line. The dashed red line displays the fitted absorption profile that is used to calculate the associated Doppler velocity of the He I 10830 Å line core. **(b)** A time-distance map of the He I 10830 Å line core Doppler velocities, saturated between ± 6 km/s for clarity, with the vertical dashed pink line highlighting the location of the persistent red-shifted brightening that segregates the umbra into two separate regions.



Extended Data Fig. 2 | Segregating the sunspot into two umbrae as a result of a persistent filamentary structure. (a) An IBIS Ca II 8542 Å line core image of the NOAA 12565 sunspot, identical to that displayed in Fig. 1e, only now with a dashed blue box highlighting a sub-field that is magnified in panel (b). It is clear to see the persistent chromospheric umbral brightening in panel (b), which is marked using a pink cross. (c) The time-averaged Stokes I/I_c intensities along the length of the umbra (extracted along the solid green line in panels a & b), with the vertical dashed pink line marking the position of the persistent chromospheric umbral brightening. The shaded green and blue regions highlight the umbral regions south and north, respectively, of the umbral brightening, with the vertical dashed red lines indicating the centres of gravity of the time-averaged Stokes I/I_c intensities for each isolated umbral region.



Extended Data Fig. 3 | Spatially resolved spectral energies across the diameter of the sunspot. Fourier spectral energy, in units of km^2/s^2 , plotted as a function of frequency and distance across the sunspot umbra. The distance corresponding to the persistent umbral brightening, which isolates the umbra into two distinct regions, is indicated by the horizontal dashed pink line. The horizontal dashed green lines represent the barycenters of the two segregated umbral cores that are isolated by the persistent brightening (see, e.g., Extended Data Fig. 2b). The dotted black line traces the weighted spectral energy centroid (in the range of 3 – 17 mHz) across the entire diameter of the sunspot umbra. This panel is a two-dimensional representation of Fig. 2d, which now preserves information along the spatial diameter of the sunspot umbra.



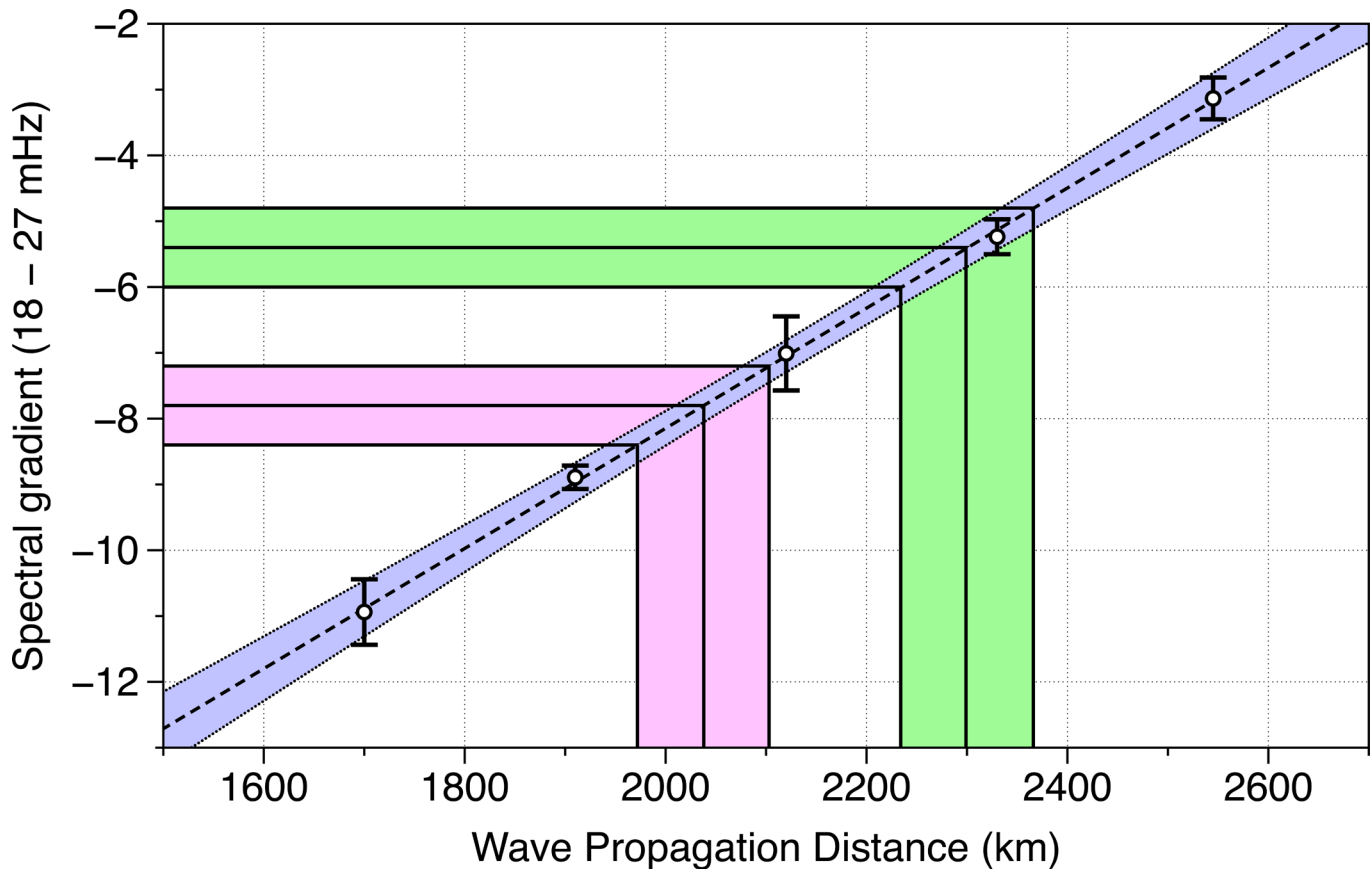
Extended Data Fig. 4 | Temperature stratification along the motion path of the simulated wave propagation. Temperature plotted as a function of wave propagation distance for 5 different stratification models. The solid black line represents the sunspot mode^[50] 'M' that has been scaled using outputs from the HAZEL inversions applied to the spectropolarimetric He I 10830 Å data products. The shaded grey region highlights the depth of the embedded resonance cavity along the motion path of the propagating magnetoacoustic waves, which can be visualized as extending from 0 km to the steep temperature gradient associated with the transition region. Here, the wave path spans a distance of 2120 km, which for vertical magnetic fields (i.e., $\cos \theta = 1$) also corresponds to the upper geometric height of the chromosphere (i.e., 2120 km as indicated by the vertical black dotted line). The blue, orange, green and purple lines depict re-scaled sunspot atmospheres with the depth of the chromospheric resonance cavities resized by 80%, 90%, 110% and 120%, respectively. As before, the coloured vertical dotted lines highlight the upper chromospheric boundary for each re-scaled umbral atmosphere.

Stratification model	Colour of line in Extended Data Fig. 4	Propagation distance along the resonance cavity (km)	Spectral gradient (18 – 27 mHz) ^a	True geometric height (km) ^b
Re-scaled 80%	blue	1700	-10.9 ± 0.5	$1700 \cos \theta$
Re-scaled 90%	orange	1910	-8.9 ± 0.2	$1910 \cos \theta$
Scaled model ⁷⁸ ‘M’	black	2120	-7.0 ± 0.6	$2120 \cos \theta$
Re-scaled 110%	green	2330	-5.2 ± 0.3	$2330 \cos \theta$
Re-scaled 120%	purple	2545	-3.1 ± 0.3	$2545 \cos \theta$

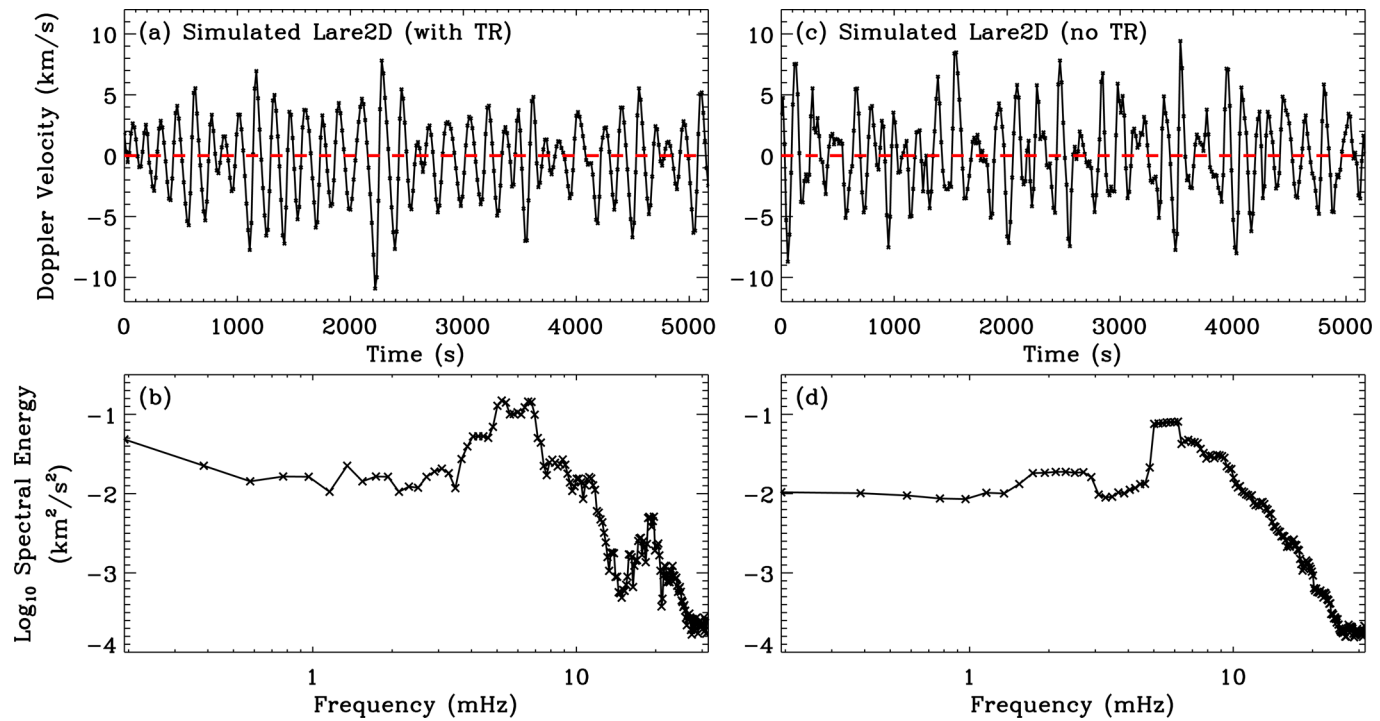
^a Plotted as a function of the wave propagation distance in Extended Data Fig. 6.

^b $\cos \theta$ is the inclination angle between the magnetic field line and the solar normal.

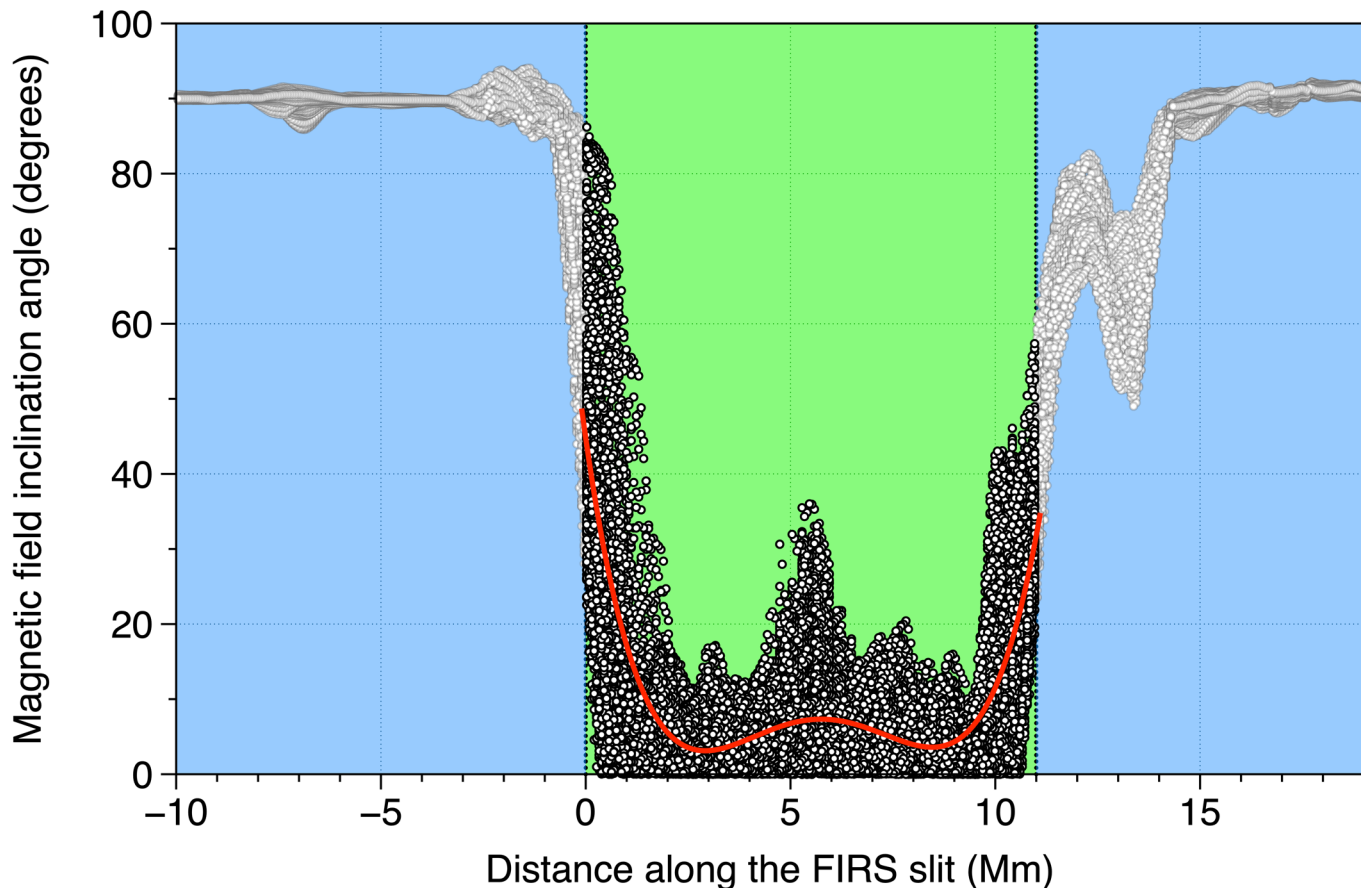
Extended Data Fig. 5 | Overview of the data-driven model atmospheres used to synthesise MHD wave activity in a sunspot. Stratified temperature models used as inputs for the Lare2D MHD code to synthesise the propagation and amplification of magnetoacoustic waves manifesting in the chromospheric resonant layers of a sunspot atmosphere. Note that the propagation distance corresponds to the physical distance covered by the propagating magnetoacoustic waves between a height of 0 km and the point when they experience a large temperature gradient (i.e., the commencement of the transition region; see the vertical dotted lines in Extended Data Fig. 4). For a vertically orientated magnetic field line, this also corresponds to the true geometric height of the upper chromosphere. However, if the magnetic field line that the magnetoacoustic waves propagate along is inclined to the solar normal (i.e., $\cos \theta \neq 1$), then this angle needs to be factored into the estimate of the true geometric height (see Equation 1 in the main text).



Extended Data Fig. 6 | Synthesised spectral gradients for region III (18 – 27 mHz) computed with the Lare2D MHD code. The spectral slopes of region III (18 – 27 mHz), which are calculated from the maximum-likelihood fits of the Fourier spectral energy produced by Lare2D numerical simulations, as a function of the variable resonance depths imposed in the modelled atmospheres. The vertical error bars highlight the maximum-likelihood 1σ fit uncertainties achieved when measuring the corresponding spectral power-law gradients. The dashed black line maps the linear best-fit line through the data points, while the blue shaded region (bounded by the black dotted lines) highlights the 95% confidence level associated with the fitted line. The shaded green and magenta regions (bounded and centred using solid black lines) highlight sample spectral gradients measured in the observational He I 10830 Å spectral energies, which can be converted into wave propagation distances through the resonance cavity. Note that these wave propagation distances also correspond to the height of the upper chromospheric boundary providing the magnetic field lines are vertically orientated.



Extended Data Fig. 7 | Comparison of spectral energies for Lare2D numerical simulations with and without an upper temperature gradient. (a & b) The simulated velocity time series, which is extracted from the Lare2D computational domain (including the steep transition region temperature gradient; see Extended Data Fig. 4) at an atmospheric height that is compatible with the formation of the He I 10830 Å spectral line, along with its corresponding spectral energy. These two panels are identical to Fig. 2e,f. (c & d) Identical information to panels (a) and (b), only now displaying the velocity time series and spectral energy corresponding to the Lare2D model atmosphere containing no upper transition region temperature gradient (i.e., a flat \sim 5000 K temperature profile from 1300 km upwards). Of particular note in panel (d) is the lack of a spectral energy enhancement at \sim 20 mHz, which is only produced in the presence of a resonance cavity. The dashed red lines (panels a and c) highlight a zero velocity for visual reference.



Extended Data Fig. 8 | Magnetic field inclination angles derived from HAZEL inversions of the He I 10830 Å spectropolarimetric data. Inclination angles, with respect to the solar normal, are plotted as a function of distance along the FIRS slit. The distance axis has been scaled to match that of Extended Data Fig. 2c, where '0 Mm' highlights the beginning of the southernmost chromospheric umbra. The grey data points and blue shaded regions indicate locations not employed in the present study, while the black data points and green shaded region (bounded by vertical dotted lines) represent the umbral pixels used to calculate the true geometric extent of the sunspot chromosphere. The green shaded region hosts 35,653 inclination angles (101 pixels across the umbra and 353 time-resolved spectra), which are fitted using a fourth-order polynomial trend line (solid red line) to establish the dominant inclination angles experienced across the umbrae.